

Optimal Angle of Attack Control for Aerocapture Maneuvers

Joshua K. Geiser* and Daniel A. Matz†
NASA Johnson Space Center, Houston, TX 77058

Recent investigations of aerocapture maneuvers have considered direct force control as a promising alternative to bank angle control. By modulating the angle of attack and sideslip angle independently, the longitudinal and lateral channels can be decoupled and thus solved separately. However, the optimal angle of attack profile for minimizing post-atmospheric propellant expenditure was previously unknown. This research applies principles of optimal control theory to numerically solve for the optimal angle of attack profile for control of the longitudinal channel. Direct methods are first employed to discretize the angle of attack profile and show that an optimal solution follows a nearly bang-bang (full lift up then full lift down) structure under a variety of conditions along the flight path angle corridor. To corroborate these results, indirect methods were also applied to scope the Optimal Control Problem (OCP) as a Two Point Boundary Value Problem (2P-BVP) which could then be solved numerically. The indirect optimization results aligned closely with the direct results, providing further evidence that a bang-bang structure provides a good approximation for the optimal angle of attack profile for aerocapture maneuvers using direct force control.

I. Introduction

EROSASSIST problems encompass a family of maneuvers that take advantage of aerodynamic forces in order to alter a spacecraft's orbit. Aerocapture is one such example of an aeroassist maneuver, where a spacecraft redirects its trajectory by flying through a planet's atmosphere (most commonly from a hyperbolic approach) to attain a desired orbit after atmospheric exit, typically at a fraction of the propellant cost. Bank angle modulation is a well-studied method for control of aeroassist maneuvers, including aerocapture. However, it leads to an inherent coupling of the longitudinal (downrange) and lateral (crossrange) channels. The longitudinal channel affects the size and shape of the resulting orbit, while the lateral channel affects the orientation of the orbital plane. Guidance schemes generally prioritize control of the longitudinal channel through the magnitude of the bank angle command, leaving the sign of the bank angle as the only control for the lateral channel. This requires the use of bank reversals to manage crossrange errors.

Direct Force Control (DFC) has recently gained research interest as a promising new alternative to bank angle control [1]. By independently controlling the angle of attack, α , and sideslip angle, β , the longitudinal and lateral channels can be decoupled and commanded separately. The longitudinal channel is controlled by varying α while the lateral channel is controlled with β . Channel prioritization is no longer necessary, as control of the longitudinal channel does not come at the expense of limited control of the lateral channel (assuming small α and β angles). Instead, it has been shown that a simple proportional-derivative (PD) controller is effective in minimizing cross-track errors in the lateral channel [2]. However, the optimal angle of attack profile α^* for minimizing post-atmospheric propellant expenditure has not been solved for in the literature.

Figure 1 depicts an in-plane schematic of a reference aerocapture trajectory. Aerodynamic controls are applied during the atmospheric pass to alter the post-atmospheric orbital parameters. Two maneuvers are then applied after atmospheric exit to correct the post-atmospheric trajectory to that of the targeted orbit. Note that any out-of-plane errors are neglected in this analysis to focus attention on the longitudinal channel.

Since spacecraft propellant (and therefore ΔV) is a limited resource, a common goal is to design a trajectory that minimizes ΔV usage. As such, in this paper an optimal aerocapture trajectory will be defined as one that minimizes the total ΔV (sum of maneuvers) required to correct the post-atmospheric trajectory to the desired orbit.

A ΔV -optimal solution for aerocapture problems using bank angle control is known to follow a bang-bang profile [3]. The bank angle is first commanded such that the vehicle flies a full-lift-up configuration, then at some calculated switching time the bank angle is reversed to its maximum value to generate a full-lift-down configuration.

Recent research has attempted to find a similar optimal solution for aerocapture maneuvers using direct force control. One study showed that the same principles of optimal control theory which provided an analytical expression for the

*Aerospace Engineer, Flight Mechanics and Trajectory Design Branch

†Aerospace Engineer, Flight Mechanics and Trajectory Design Branch, AIAA Senior Member

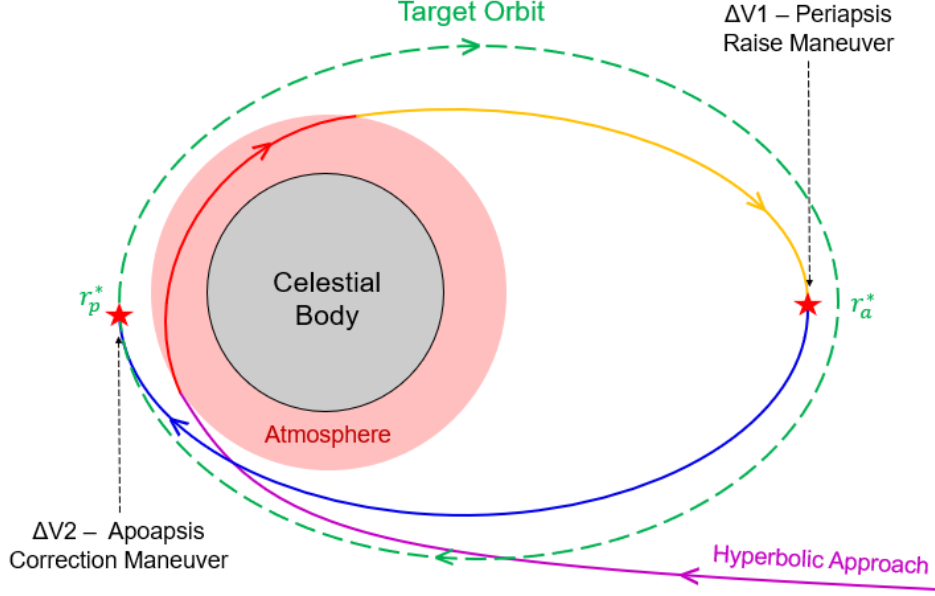


Fig. 1 Example Aerocapture Trajectory. After a hyperbolic approach, the spacecraft dissipates velocity by flying through the planet's atmosphere, entering into a captured orbit. $\Delta V1$ raises the periapsis to the targeted value, r_p^* . A second maneuver is applied at periapsis (if needed) to correct any error in the target apoapsis, r_a^* .

optimal bank angle, σ^* , as in Ref. [3], do not yield an analytical solution for the optimal angle of attack command when using DFC [2]. Another study found that under the assumption of a linear aerodynamics model, the optimal angle of attack command follows a bang-bang profile [4]. However, coefficient of drag for blunt bodies, C_D , varies quadratically with angle of attack, thus a linearized aerodynamics model is not sufficient for capturing the full dynamical behavior in aerocapture maneuvers. A third study cast the Optimal Control Problem (OCP) as a minimum-time problem and then used numerical techniques to solve for the optimal angle of attack profile [5]. However, a minimum-time objective function provides little insight into how ΔV optimality varies with respect to the commanded angle of attack.

This paper seeks to build off of previous work by numerically solving for the ΔV -optimal angle of attack profile using a more representative aerodynamics model. First, relevant equations of motion for atmospheric flight are presented to provide a mathematical basis for aerocapture problems using either bank angle control or DFC. Next, principles of optimal control theory are applied to provide expressions for solving the open-loop OCP using both direct and indirect methods. Commercial solvers are then used to numerically solve the OCP for the optimal angle of attack profile. Last, numerical results are shown to give insight into the ΔV -minimizing angle of attack profile when using DFC.

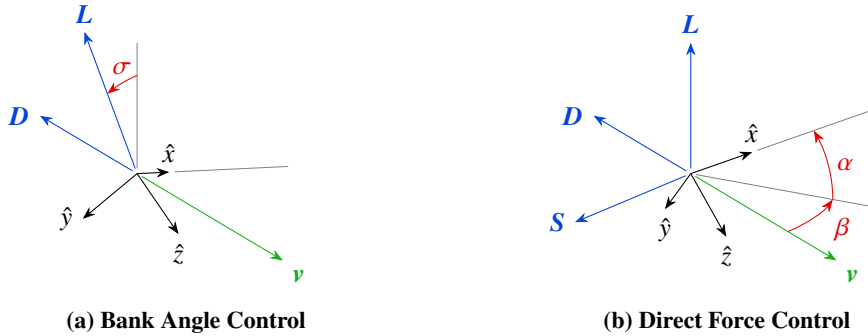


Fig. 2 Comparison of geometry between Bank Angle Control and Direct Force Control. Vehicle axes are shown in black, aerodynamic forces are in blue, velocity is in green, and control variables are in red.

II. Background

Analysis of the optimal angle of attack profile requires a mix of atmospheric flight mechanics, Keplerian orbital mechanics, and optimal control theory. This section provides the reader with a background of the relevant equations of motion for this problem. Also included here is a succinct review of previous work that has focused on deriving closed-form expressions for optimal aerocapture trajectories. The lack of a known analytical expression for the optimal angle of attack profile, as discussed below, further motivates the use of numerical techniques to determine the optimal profile.

A. Equations of Motion

Assuming a spherical gravity model and neglecting planetary rotation, the longitudinal equations of motion for atmospheric flight are given as follows:

$$\dot{r} = v \sin \gamma \quad (1)$$

$$\dot{v} = -\frac{D}{m} - \frac{\mu \sin \gamma}{r^2} \quad (2)$$

$$\dot{\gamma} = \frac{1}{v} \left[\frac{L \cos \sigma}{m} + \left(v^2 - \frac{\mu}{r} \right) \frac{\cos \gamma}{r} \right] \quad (3)$$

where r is the radial distance from the center of the planetary body, v is the inertial velocity magnitude, γ is the flight path angle (FPA) of the velocity vector, σ is the vehicle bank angle, μ is the gravitational parameter of the attracting body, L and D are the lift and drag forces of the vehicle, respectively, and m is the vehicle mass.

The lift and drag forces are defined as:

$$L = \frac{1}{2} \rho v^2 S C_L \quad (4)$$

$$D = \frac{1}{2} \rho v^2 S C_D \quad (5)$$

where ρ is the atmospheric density, S is the vehicle reference area, and C_L and C_D are the coefficients of lift and drag, respectively. Both C_L and C_D are functions of the angle of attack, α , and sideslip angle, β . However, to simplify the analysis we will assume that β is small, thus the influence of β on C_L and C_D is weak and we will neglect it. These coefficients are then defined as:

$$C_L = C_{L_1} \alpha + C_{L_0} \quad (6)$$

$$C_D = C_{D_2} \alpha^2 + C_{D_1} \alpha + C_{D_0} \quad (7)$$

where C_{L_1} , C_{L_0} , C_{D_2} , C_{D_1} , and C_{D_0} are constants determined by the vehicle geometry. Here we have assumed that C_L varies linearly with α and C_D varies quadratically with α , which is reasonable for a blunt-bodied vehicle flying at low α .

By assuming two-body Keplerian orbital mechanics after atmospheric exit, the post-atmospheric orbital parameters are a function of the state variables solely at the exit condition. The apoapsis and periapsis radii are given as:

$$r_a = a \left(1 + \sqrt{\frac{1 - v_f^2 r_f^2 \cos^2(\gamma_f)}{\mu a}} \right) \quad (8)$$

$$r_p = a \left(1 - \sqrt{\frac{1 - v_f^2 r_f^2 \cos^2(\gamma_f)}{\mu a}} \right) \quad (9)$$

where r_f , v_f , and γ_f are the state variables at atmospheric exit, and the semi-major axis a is given by:

$$a = \frac{\mu}{2\mu/r_f - v_f^2} \quad (10)$$

With knowledge of the post-atmospheric periapsis and apoapsis radii (r_a and r_p) as well as the desired orbital parameters (r_a^* and r_p^*), the ΔV required for insertion into the target orbit can be calculated. Two different formulations

for calculating ΔV will be used throughout this paper. The first formulation will assume that the desired apoapsis radius, r_a^* , is explicitly targeted such that it is equal to the apoapsis radius at atmospheric exit: $r_a = r_a^*$. In this formulation, only one impulsive burn is needed in order to raise the periapsis radius above the atmosphere to the desired value, r_p^* . The total required ΔV for the one-burn formulation is then:

$$J_1 = |\Delta V_1| = \sqrt{2\mu} \left(\left| \sqrt{\frac{1}{r_a^*} - \frac{1}{r_a^* + r_p^*}} - \sqrt{\frac{1}{r_a^*} - \frac{1}{2a}} \right| \right) \quad (11)$$

The second formulation assumes that the desired apoapsis radius is *not* explicitly targeted, thus two impulsive burns are needed to correct to the desired orbit. The total required ΔV for the two-burn formulation is then:

$$J_2 = |\Delta V_1| + |\Delta V_2| = \sqrt{2\mu} \left(\left| \sqrt{\frac{1}{r_a} - \frac{1}{r_a + r_p^*}} - \sqrt{\frac{1}{r_a} - \frac{1}{2a}} \right| + \left| \sqrt{\frac{1}{r_p^*} - \frac{1}{r_a^* + r_p^*}} - \sqrt{\frac{1}{r_p^*} - \frac{1}{r_a + r_p^*}} \right| \right) \quad (12)$$

B. Bank Angle Control

The ΔV -optimal bank angle command is solved for in Ref. [3], however a review of the derivation is included here to illustrate the differences between bank angle control and DFC and to motivate the use of numerical methods in the following section. The objective function of the optimal control problem takes the form of either Eq. (11) or (12), depending on whether or not the apoapsis condition is explicitly targeted. Using indirect optimization techniques, the Hamiltonian is:

$$H = \lambda_r v \sin \gamma + \lambda_v \left[-\frac{D}{m} - \frac{\mu \sin \gamma}{r^2} \right] + \lambda_\gamma \left[\frac{1}{v} \left(\frac{L \cos \sigma}{m} + \left(v^2 - \frac{\mu}{r} \right) \frac{\cos \gamma}{r} \right) \right] \quad (13)$$

where λ_r , λ_v , and λ_γ are the costate variables.

Since the bank angle command is generally bounded to lie within some range such that $\sigma_{\min} \leq |\sigma| \leq \sigma_{\max}$, Pontryagin's Minimum Principle [6] must be applied to determine the optimal bank angle command:

$$H(\mathbf{x}^*, \sigma^*, \lambda^*, t) \leq H(\mathbf{x}^*, \sigma, \lambda^*, t) \quad (14)$$

$$\frac{\lambda_\gamma^*}{v^*} L^* \cos \sigma^* \leq \frac{\lambda_\gamma^*}{v^*} L^* \cos \sigma \quad (15)$$

This yields three cases for the optimal bank angle command, σ^* , based on the value of the costate variable λ_γ^* :

$$\sigma^* = \begin{cases} \sigma_{\min} & \text{if } \lambda_\gamma^* > 0 \\ \sigma_{\max} & \text{if } \lambda_\gamma^* < 0 \\ \in [\sigma_{\min}, \sigma_{\max}] & \text{if } \lambda_\gamma^* = 0 \end{cases} \quad (16)$$

The third case, where $\lambda_\gamma^* = 0$, can be shown to not exist [3]. Therefore, the optimal bank angle command follows a bang-bang profile such that σ^* only takes the value of either σ_{\min} or σ_{\max} throughout the trajectory.

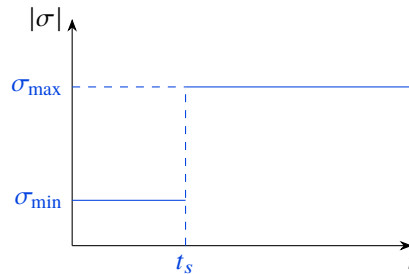


Fig. 3 Optimal bank angle command using bank angle control. At some specified switching time, t_s , the optimal bank angle command switches from σ_{\min} (full lift up) to σ_{\max} (full lift down).

C. Direct Force Control

A similar methodology is applied in Ref. [2] to attempt to solve for the optimal angle of attack command, α^* , and is included here as well. With DFC, the bank angle is set to zero and the lift and drag forces are functions of the angle of attack, therefore the Hamiltonian becomes:

$$H = \lambda_r v \sin \gamma + \lambda_v \left[-\frac{D(\alpha)}{m} - \frac{\mu \sin \gamma}{r^2} \right] + \lambda_\gamma \left[\frac{1}{v} \left(\frac{L(\alpha)}{m} + \left(v^2 - \frac{\mu}{r} \right) \frac{\cos \gamma}{r} \right) \right] \quad (17)$$

We will again assume bounded controls such that $\alpha_{\min} \leq \alpha \leq \alpha_{\max}$. Applying Pontryagin's Minimum Principle, we find:

$$H(\mathbf{x}^*, \alpha^*, \lambda^*, t) \leq H(\mathbf{x}^*, \alpha, \lambda^*, t) \quad (18)$$

$$-\lambda_v^* D(\alpha^*) + \lambda_\gamma^* \frac{L(\alpha^*)}{v^*} \leq -\lambda_v^* D(\alpha) + \lambda_\gamma^* \frac{L(\alpha)}{v^*} \quad (19)$$

With two costate variables appearing in the above expression, an analytical solution is not as easily found. For example, let's consider the case where both $\lambda_v^* > 0$ and $\lambda_\gamma^* > 0$. The two terms in the expression have opposing signs, therefore there is no intuitive value of α^* that can be easily selected to ensure that the inequality holds for all values of α . The optimal solution is not necessarily bang-bang, but could also include intermediate values of α between α_{\min} and α_{\max} . Since we cannot obtain an analytical solution for the optimal angle of attack profile, this motivates the use of numerical methods for solving the OCP. These will be discussed in the following section.

III. Problem Formulation

Two main methods exist for solving open-loop trajectory optimization problems: direct methods and indirect methods. Direct methods involve discretizing the control profile, converting the OCP into a constrained nonlinear optimization problem, and then solving using nonlinear programming. On the other hand, indirect methods involve constructing the necessary and sufficient conditions for optimality, transcribing the OCP into a Two Point Boundary Value Problem (2P-BVP), and then solving the 2P-BVP numerically. Both direct and indirect methods are applied here to solve for the optimal angle of attack profile, and results between the two methodologies are compared for cross-validation purposes.

A. Direct Methods

A variety of different discretization strategies were applied to attempt to solve the OCP using direct methods. Results from each (to be shown in Section IV) motivated the application of additional approaches to corroborate results. Each of these approaches shed additional insight into the profile of the optimal trajectory.

1. Discretized Angle of Attack Profile

In this approach, the continuous angle of attack profile was discretized directly into a vector of N decision variables, where N denotes the number of discretized points. Each decision variable x_i in the vector \mathbf{x} then defines the angle of attack command at time t , where $t \in [t_0, t_f]$ and each decision variable is spaced evenly apart in time. Linear interpolation was then used to determine the angle of attack command along the $N - 1$ segments connecting the decision variables at N specified times.

The OCP could be formulated in two different ways, depending on whether or not the desired post-atmospheric apoapsis was explicitly constrained during the aerocapture maneuver. With targeting, the objective function takes the form of Eq. (11) and an additional equality constraint is imposed:

$$\begin{aligned} \text{minimize: } & |\Delta V_1(\mathbf{x})| \\ \text{subject to: } & \alpha_{\min} \leq \mathbf{x} \leq \alpha_{\max} \\ & r_a(\mathbf{x}) = r_a^* \\ & \mathbf{x} = [\alpha_1, \alpha_2, \dots, \alpha_N]^T \in \mathbb{R}^N \end{aligned} \quad (20)$$

Without apoapsis targeting, a two-burn scheme is required as in Eq. (12). The OCP is then formulated as:

$$\begin{aligned} \text{minimize: } & |\Delta V_1(\mathbf{x})| + |\Delta V_2(\mathbf{x})| \\ \text{subject to: } & \alpha_{\min} \leq \mathbf{x} \leq \alpha_{\max} \\ & \mathbf{x} = [\alpha_1, \alpha_2, \dots, \alpha_N]^T \in \mathbb{R}^N \end{aligned} \quad (21)$$

Both formulations were shown to yield identical results for the chosen target orbit parameters used in Section IV. However, the one-burn formulation demonstrated better convergence properties in practice, thus the OCP formulation as in Eq. (20) was used to attain the results in Section IV.

2. Near Bang-Bang Profile

A second discretization strategy was used to simulate a “near” bang-bang angle of attack profile. This was motivated by results of the discretized angle of attack profile (as shown in Section IV) to determine the degree to which a bang-bang profile properly reflected the true optimal profile.

In this formulation, the angle of attack profile was discretized into three segments. In the first segment, the vehicle flies at α_{\min} while in the third segment the vehicle flies at α_{\max} . The middle segment defines a transient regime where α varies linearly between α_{\min} and α_{\max} . The decision variables are no longer the discretized values of α , but are now two switching times, t_1 and t_2 , that mark the transitions between the three discrete segments. Switching times that are nearly equal imply little to no transient regime, i.e. a bang-bang profile.

The one-burn objective function (as in Eq. (11)) was primarily used, as its convergence was faster and more robust while yielding nearly identical results to a two-burn formulation. The OCP can then be defined as:

$$\begin{aligned} \text{minimize: } & |\Delta V_1(\mathbf{x})| \\ \text{subject to: } & t_0 \leq \mathbf{x} \leq t_f \\ & r_a(\mathbf{x}) = r_a^* \\ & x_1 \leq x_2 \\ & \mathbf{x} = [t_1, t_2]^T \in \mathbb{R}^2 \end{aligned} \quad (22)$$

3. Bang-Bang Profile

A fully bang-bang profile was also tested to compare ΔV results with the previous formulations using direct methods. The angle of attack profile was split into two segments, the first at α_{\min} and the second at α_{\max} . The singular decision variable in the OCP is the switching time, t_s , between the two segments. Any feasible solution to this OCP would then have a constant or bang-bang angle of attack profile. Again using a one-burn objective function, the OCP is then formulated as follows:

$$\begin{aligned} \text{minimize: } & |\Delta V_1(x)| \\ \text{subject to: } & t_0 \leq x \leq t_f \\ & r_a(x) = r_a^* \\ & x = t_s \in \mathbb{R} \end{aligned} \quad (23)$$

B. Indirect Methods

Indirect methods were also applied to the trajectory optimization problem to compare results against the direct methods and to further validate any conclusions on the optimal angle of attack profile. These methods focused on rescaling the OCP as a 2P-BVP that could be numerically solved with a commercial solver. Both a two-burn and a one-burn formulation were considered and derived here.

For the following subsections, we will consider an OCP of the following form:

$$\text{minimize: } J = \phi[\mathbf{x}(t_f), t_f] + \int_{t_0}^{t_f} L[\mathbf{x}(t), \mathbf{u}(t), t] dt \quad (24)$$

$$\text{subject to: } \dot{\mathbf{x}} = \mathbf{f}[\mathbf{x}(t), \mathbf{u}(t), t] \quad (25)$$

$$\mathbf{x}(t_0) = \mathbf{x}_0 \quad (26)$$

$$\psi[\mathbf{x}(t_f), t_f] = \mathbf{0} \quad (27)$$

where Eq. (24) is the objective function with terminal cost $\phi(\cdot)$ and path cost $\int_{t_0}^{t_f} L(\cdot) dt$, Eq. (25) is the system dynamics, and Eqs. (26) and (27) denote the initial and terminal boundary conditions, respectively. The Hamiltonian is then defined as:

$$H = L[\mathbf{x}(t), \mathbf{u}(t), t] + \lambda^T(t) \mathbf{f}[\mathbf{x}(t), \mathbf{u}(t), t] \quad (28)$$

where λ denotes the costate variables. For a feasible trajectory with unbounded controls, the necessary conditions for optimality are:

$$\dot{\mathbf{x}} = \mathbf{f}[\mathbf{x}(t), \mathbf{u}(t), t] \quad (29)$$

$$\dot{\lambda} = -\frac{\partial H}{\partial \mathbf{x}} \quad (30)$$

$$\mathbf{0} = \frac{\partial H}{\partial \mathbf{u}} \quad (31)$$

One of the more general forms an OCP can take is that of a free-end-time problem where functions of the state variables are specified at an unspecified terminal time [7]. For this case, in addition to Eqs. (29-31) above, an optimal trajectory must also satisfy a set of additional constraints imposed by the boundary conditions. Assuming a given initial state, these conditions are:

$$\mathbf{x}(t_0) = \mathbf{x}_0 \quad (32)$$

$$\lambda(t_f) = \left(\frac{\partial \phi}{\partial \mathbf{x}} + \nu^T \frac{\partial \psi}{\partial \mathbf{x}} \right)_{t=t_f}^T \quad (33)$$

$$0 = \left[\frac{\partial \phi}{\partial t} + \nu^T \frac{\partial \psi}{\partial t} + \left(\frac{\partial \phi}{\partial \mathbf{x}} + \nu^T \frac{\partial \psi}{\partial \mathbf{x}} \right) \mathbf{f} + L \right]_{t=t_f} \quad (34)$$

$$\mathbf{0} = \psi[\mathbf{x}(t_f), t_f] \quad (35)$$

where ν denotes a vector of parameters used to enforce the terminal boundary condition given by Eq. (35). Note that these equations are very general and simplify for more specific OCP formulations. For example, if some or all state variables are explicitly specified at an unspecified terminal time (as opposed to *functions* of the state variables), Eq. (34) collapses to the form $\left(\frac{\partial \phi}{\partial t} + H \right)_{t=t_f} = 0$, and is removed entirely for a fixed-end-time problem. Eqs. (29-35) are used in defining the 2P-BVPs below.

1. Fixed-End-Time, 2-Burn Formulation

The OCP was first constructed using a two-burn formulation (i.e. objective function equal to Eq. (12)) with a fixed end time. By using a fixed end time, results could be more directly compared with that of the direct methods by numerically integrating over the same time interval as the direct method results to see if the same profile is achieved. Assuming a fixed end time also provides one less variable to be numerically solved for, thus narrowing the search space for the 2P-BVP solver.

Since only the longitudinal channel is considered here, we will define our state vector as $\mathbf{x} = (r, v, \gamma)^T$. Adjoining the costate variables, our state vector becomes $\mathbf{x} = (r, v, \gamma, \lambda_r, \lambda_v, \lambda_\gamma)^T$. Eqs. (29-30) define the state dynamics for this system. Eq. (31) is valid only in the case of unbounded control, however we generally have a bounded control such that $\alpha_{\min} \leq \alpha \leq \alpha_{\max}$. To account for this, we will use principles from the Unified Trigonometrization Method (UTM) to rescale our control variable as an unbounded control [5]. We will perform the substitutions:

$$\alpha_0 = \frac{\alpha_{\max} + \alpha_{\min}}{2} \quad (36)$$

$$\alpha_1 = \frac{\alpha_{\max} - \alpha_{\min}}{2} \quad (37)$$

$$\alpha = \alpha_1 \sin \bar{\alpha} + \alpha_0 \quad (38)$$

where $\bar{\alpha}$ is our new control and is inherently bounded due to the use of trigonometric functions. Applying Eq. (31):

$$\begin{aligned} \frac{\partial H}{\partial \bar{\alpha}} &= \frac{\partial}{\partial \bar{\alpha}} \left(\lambda_r v \sin \gamma + \lambda_v \left[-\frac{D(\bar{\alpha})}{m} - \frac{\mu \sin \gamma}{r^2} \right] + \lambda_\gamma \left[\frac{1}{v} \left(\frac{L(\bar{\alpha})}{m} + \left(v^2 - \frac{\mu}{r} \right) \frac{\cos \gamma}{r} \right) \right] \right) \\ &= \left[-v \lambda_v (2C_{D_2}(\alpha_1 \sin \bar{\alpha} + \alpha_0) + C_{D_1}) + \lambda_\gamma C_{L_1} \right] \cos \bar{\alpha} \\ &= 0 \end{aligned} \quad (39)$$

Eq. (39) has three solutions for $\bar{\alpha}$. Using the substitutions in Eqs. (36-38), we can transcribe our three solutions back into our original control variable:

$$\alpha^* = \begin{cases} \alpha_{\min} \\ \frac{1}{2C_{D_2}} \left(\frac{C_{L_1}\lambda_y}{v\lambda_v} - C_{D_1} \right) \\ \alpha_{\max} \end{cases} \quad (40)$$

We can now calculate the Hamiltonian for each of the listed control options and apply Pontryagin's Minimum Principle as in Eq. (18) to select the optimal control law.

For terminal boundary conditions, we will enforce that $r(t_f) = r_f$, i.e. the vehicle must reach the atmospheric exit altitude corresponding to r_f at the final time t_f . In this formulation we now have a system where some state variables are specified at a fixed terminal time. This leads to a simplification of Eqs. (33-35). Since we are dealing with a fixed terminal time problem, Eq. (34) is no longer necessary. Additionally, since we have some state variables explicitly specified (rather than having *functions* of state variables specified), Eq. (33) reduces to:

$$\lambda(t_f) = \left(\frac{\partial \phi}{\partial \mathbf{x}} \right)_{t=t_f}^T \quad (41)$$

The above equation is only enforced for costate variables that do not have a terminal constraint on their corresponding state variable. Since $r(t_f)$ is constrained, only $\lambda_v(t_f)$ and $\lambda_\gamma(t_f)$ will have terminal costate constraints.

Putting all of this together, our 2P-BVP now evolves with dynamics:

$$\begin{bmatrix} \dot{r} \\ \dot{v} \\ \dot{\gamma} \\ \dot{\lambda}_r \\ \dot{\lambda}_v \\ \dot{\lambda}_\gamma \end{bmatrix} = \begin{bmatrix} v \sin \gamma \\ -\frac{D(\alpha)}{m} - \frac{\mu \sin \gamma}{r^2} \\ \frac{1}{v} \left[\frac{L(\alpha)}{m} + (v^2 - \frac{\mu}{r}) \frac{\cos \gamma}{r} \right] \\ -\frac{\partial H}{\partial r} \\ -\frac{\partial H}{\partial v} \\ -\frac{\partial H}{\partial \gamma} \end{bmatrix} \quad (42)$$

and must meet boundary conditions given by:

$$\begin{bmatrix} r(t_0) - r_0 \\ v(t_0) - v_0 \\ \gamma(t_0) - \gamma_0 \\ r(t_f) - r_f \\ \lambda_v(t_f) - (\partial \phi / \partial v)_{t=t_f} \\ \lambda_\gamma(t_f) - (\partial \phi / \partial \gamma)_{t=t_f} \end{bmatrix} = \mathbf{0} \quad (43)$$

In this formulation, ϕ takes the form of Eq. (12). The initial state is specified by r_0 , v_0 , and γ_0 , and the final vehicle radius is specified by r_f . The UTM method, as described previously, is used at each timestep to select the commanded angle of attack α^* . Automatic differentiation is used to calculate the partial derivatives in Eqs. (42) and (43) to avoid lengthy analytical derivations. An optimal solution to the 2P-BVP is one that satisfies the above dynamics equations while also meeting the specified boundary conditions.

2. Free-End-Time, 1-Burn Formulation

In this subsection, the OCP is reformulated as a free-end-time problem with a targeted apoapsis condition. Having a free end time is a more realistic problem formulation since the optimal time interval is not typically known a priori. Additionally, a one-burn formulation ensures that the desired post-atmospheric apoapsis altitude is met, and results can be compared with the two-burn case to see if both formulations yield the same result.

To account for the free end time, we will augment the state vector with an additional variable representing the final time: $\mathbf{x} = (r, v, \gamma, \lambda_r, \lambda_v, \lambda_\gamma, t_f)^T$. Since the final time is simply a constant, it will have trivial dynamics $\dot{t}_f = 0$. We will also introduce a change of variables $\tau = t/t_f$ to rescale our time interval. This rescaling ensures that our numerical

integration interval will be from $\tau = 0$ to $\tau = 1$. However, we must be careful to also rescale our dynamics due to the effect of our change of variables on derivatives:

$$\frac{d}{d\tau} = t_f \frac{d}{dt} \quad (44)$$

$$\begin{aligned} \dot{\mathbf{x}} &= \frac{d\mathbf{x}}{d\tau} \\ &= t_f \frac{d\mathbf{x}}{dt} \\ &= t_f \mathbf{f}(\mathbf{x}, \mathbf{u}, t) \end{aligned} \quad (45)$$

Our terminal boundary conditions are now slightly more complicated due to the apoapsis targeting condition, which can be calculated as a function of the terminal state. We now have:

$$\boldsymbol{\psi}[\mathbf{x}(t_f), t_f] = \begin{bmatrix} r(t_f) - r_f \\ r_a[\mathbf{x}(t_f)] - r_a^* \end{bmatrix} = \mathbf{0} \quad (46)$$

Next, we will define:

$$\Phi = \phi + \mathbf{v}^T \boldsymbol{\psi} \quad (47)$$

$$= \phi + v_1(r(t_f) - r_f) + v_2(r_a[\mathbf{x}(t_f)] - r_a^*) \quad (48)$$

If we differentiate with respect to each of our state variables, we arrive at Eq. (33), our terminal costate conditions. Since $r(t_f)$ is specified, we need only worry about $\lambda_v(t_f)$ and $\lambda_\gamma(t_f)$:

$$\lambda_v(t_f) = \left(\frac{\partial \phi}{\partial v} \right)_{t=t_f} + v_2 \left(\frac{\partial r_a}{\partial v} \right)_{t=t_f} \quad (49)$$

$$\lambda_\gamma(t_f) = \left(\frac{\partial \phi}{\partial \gamma} \right)_{t=t_f} + v_2 \left(\frac{\partial r_a}{\partial \gamma} \right)_{t=t_f} \quad (50)$$

The unknown parameter v_2 can be removed by consolidating the above two equations into a single boundary condition:

$$\lambda_v(t_f) = \left(\frac{\partial \phi}{\partial v} \right)_{t=t_f} + \left[\lambda_\gamma(t_f) - \left(\frac{\partial \phi}{\partial \gamma} \right)_{t=t_f} \right] \frac{(\partial r_a / \partial v)_{t=t_f}}{(\partial r_a / \partial \gamma)_{t=t_f}} \quad (51)$$

The last consideration to take into account is that we have one additional boundary condition due to the free terminal time. However, for our case Eq. (34) simplifies to $H(t_f) = 0$, which is our last boundary condition.

To summarize, our 2P-BVP has dynamics:

$$\begin{bmatrix} \dot{r} \\ \dot{v} \\ \dot{\gamma} \\ \dot{\lambda}_r \\ \dot{\lambda}_v \\ \dot{\lambda}_\gamma \\ \dot{i}_f \end{bmatrix} = t_f \begin{bmatrix} v \sin \gamma \\ -\frac{D(\alpha)}{m} - \frac{\mu \sin \gamma}{r^2} \\ \frac{1}{v} \left[\frac{L(\alpha)}{m} + (v^2 - \frac{\mu}{r}) \frac{\cos \gamma}{r} \right] \\ -\frac{\partial H}{\partial r} \\ -\frac{\partial H}{\partial v} \\ -\frac{\partial H}{\partial \gamma} \\ 0 \end{bmatrix} \quad (52)$$

and must meet boundary conditions:

$$\begin{bmatrix} r(t_0) - r_0 \\ v(t_0) - v_0 \\ \gamma(t_0) - \gamma_0 \\ r(t_f) - r_f \\ -\lambda_v(t_f) + \left(\frac{\partial \phi}{\partial v} \right)_{t=t_f} + \left[\lambda_\gamma(t_f) - \left(\frac{\partial \phi}{\partial \gamma} \right)_{t=t_f} \right] \frac{(\partial r_a / \partial v)_{t=t_f}}{(\partial r_a / \partial \gamma)_{t=t_f}} \\ H(t_f) \end{bmatrix} = \mathbf{0} \quad (53)$$

where r_0 , v_0 , γ_0 , and r_f are given constants. The UTM method is still used to calculate the optimal angle of attack command at each timestep. Automatic differentiation is also applied here to simplify partial derivative calculations. An optimal solution to this 2P-BVP must satisfy both the dynamics constraints and the boundary conditions.

IV. Numerical Results

With multiple formulations derived for both direct and indirect methods, these methodologies could be implemented and compared using various numerical solvers. Julia programming language was used to complete this analysis [8]. The DifferentialEquations.jl package was used for numerical integration of the equations of motion, as well as for solving the 2P-BVPs with a shooting method [9]. SNOPT was used as an off-the-shelf nonlinear optimizer for the direct methods [10].

Mars aerocapture was the focus of this study, however these results could be repeated for any body with a non-negligible atmosphere. Table 1 specifies the vehicle properties and other parameters used for this numerical analysis. These properties are representative of a blunt-bodied low L/D vehicle with a narrow range for commanded angle of attack. For these parameters and for the given target orbit, the FPA corridor was calculated to have a range approximately 1° wide. A scan across various FPAs was conducted to assess how the angle of attack profile varied across this corridor.

Table 1 Parameters Used for Numerical Analysis

Parameters	Values	
Target Orbit	$h_p^* = 250\text{km}$,	$h_a^* = 500\text{km}$
Angle of Attack Bounds	$\alpha_{\min} = -9.51^\circ$,	$\alpha_{\max} = +9.51^\circ$
Flight Path Angle Corridor	$\gamma_{\min} = -10.9^\circ$,	$\gamma_{\max} = -9.9^\circ$
Vehicle Properties	$m = 55000\text{kg}$,	$S = 211.24\text{m}^2$
Lift Coefficients	$C_{L_0} = -0.00458$,	$C_{L_1} = -1.37475$
Drag Coefficients	$C_{D_0} = +1.71363$,	$C_{D_1} = -0.11747$, $C_{D_2} = -3.18429$
Initial Conditions	$h_0 = 125\text{km}$,	$v_0 = 6199.985\text{m/s}$, $\gamma_0 \in [\gamma_{\min}, \gamma_{\max}]$
Terminal Condition(s)	$h_f = 125\text{km}$,	$h_{a,f} = h_a^*$ (1-burn case)

A. Direct Methods Results

All three direct method approaches defined in Section III were run here: a fully discretized angle of attack profile, a near bang-bang profile, and a bang-bang profile. Additionally, for each approach, a scan across three different flight path angle values was conducted throughout the flight path angle corridor: a steep FPA ($\gamma_0 = -10.8^\circ$), a moderate FPA ($\gamma_0 = -10.4^\circ$), and a shallow FPA ($\gamma_0 = -10.0^\circ$). Each plot in this section includes both the optimized angle of attack profile as well as the dynamic pressure curve throughout the atmospheric pass. The dynamic pressure curve is coplotted to better illustrate when the angle of attack command has the most aerodynamic control authority (i.e. the angle of attack command will have little to no effect on vehicle trajectory when dynamic pressure is close to zero).

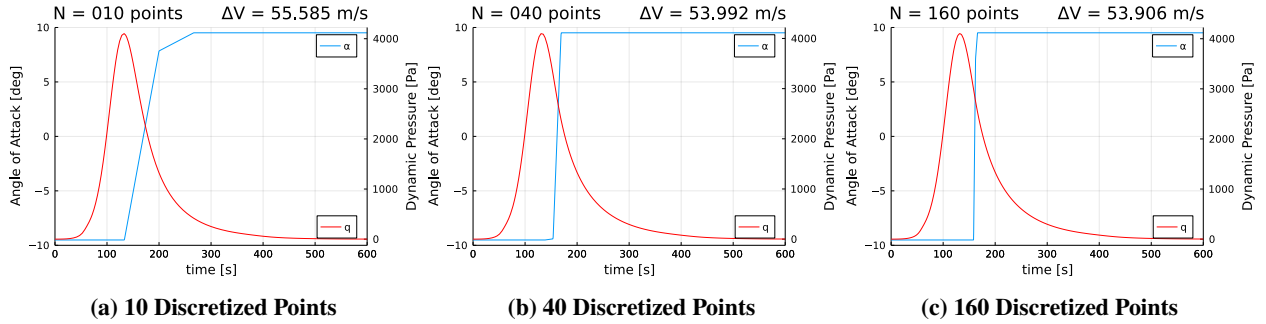


Fig. 4 Fully Discretized Angle of Attack Profile with Steep FPA

Figure 4 compares different numbers of discretization points for a steep FPA case. As can be seen, for increasing numbers of discretized points, the optimal profile appears to approach that of a bang-bang profile. Additionally, ΔV tends to decrease for increasing discretization points, providing evidence that a bang-bang profile is indeed more optimal.

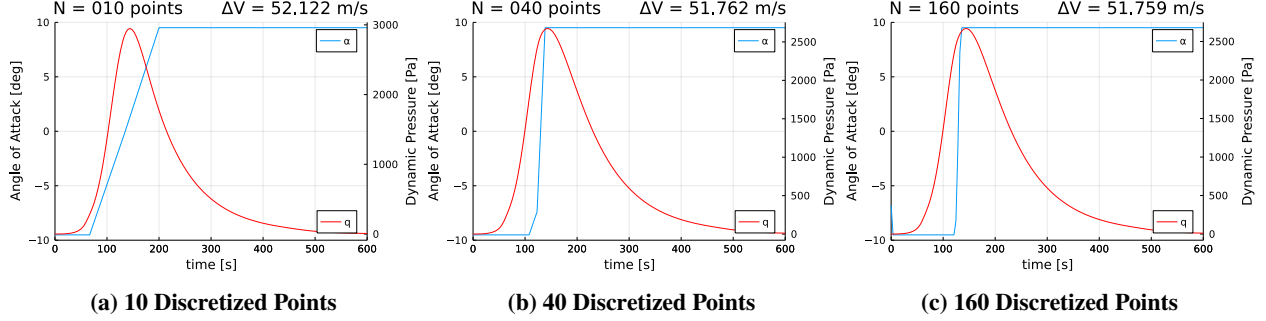


Fig. 5 Fully Discretized Angle of Attack Profile with Moderate FPA

In Figure 5, a moderate FPA is used to compare the effect of a varying number of discretization points. We again notice that for an increasing number of discretized points, the ΔV decreases and the profile approaches a bang-bang structure. We can also see that, compared to the steep FPA case, the switching time (from α_{\min} to α_{\max}) now occurs earlier in the dynamic pressure curve and the total ΔV is lower. This aligns with intuition, as a more moderate FPA leads to a higher periapsis, thus less ΔV is needed to raise it to the desired periapsis altitude.

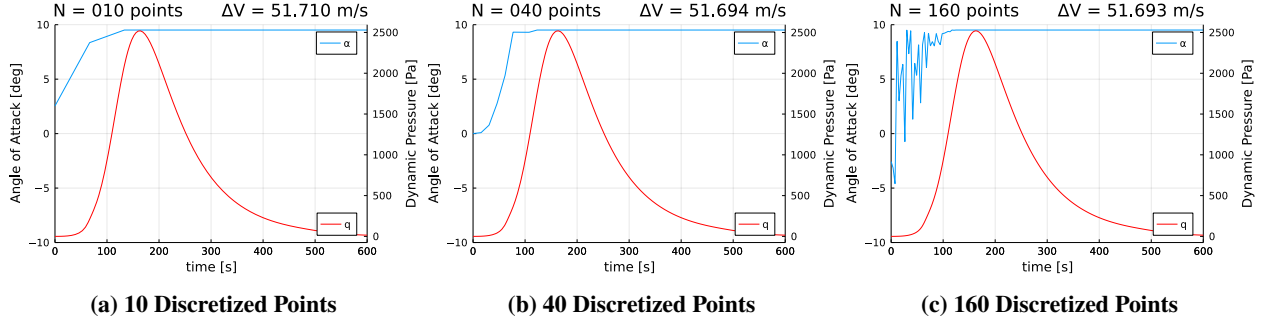


Fig. 6 Fully Discretized Angle of Attack Profile with Shallow FPA

Figure 6 provides a comparison for the shallow FPA case. We now notice that, contrary to the steep and moderate FPA cases, the angle of attack profile here does not appear to be bang-bang. However, we can observe that the irregular nature of the angle of attack plots (especially for $N = 160$) is an indication of potential numerical difficulties. This can likely be attributed to the fact that the majority of the transient period of the angle of attack command occurs very early on in the dynamic pressure curve, when the vehicle has little to no aerodynamic control authority.

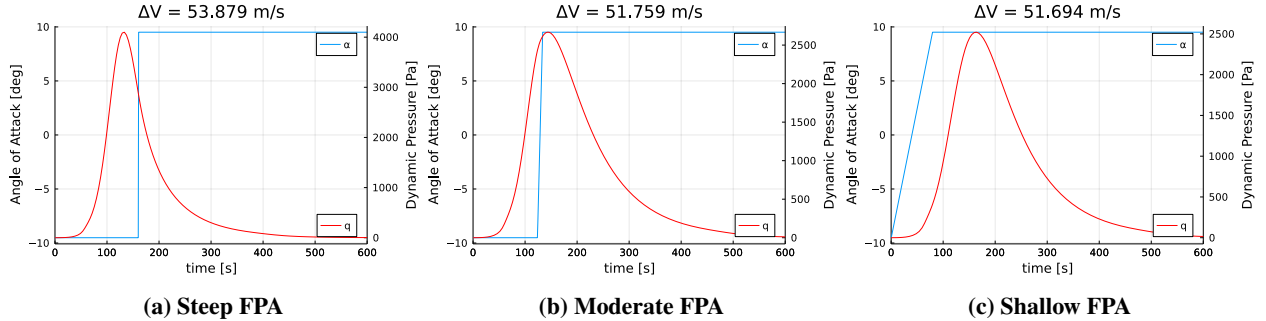


Fig. 7 Near Bang-Bang Profile with Various FPAs

The ambiguity of the shallow FPA result, combined with the evidence of a clear bang-bang structure for the steep and moderate FPA cases, motivated the use of additional approaches for comparison purposes. Results from the second approach, the near bang-bang profile approach, are shown in Figure 7. As can be seen, the steep and moderate FPA plots show further evidence of a bang-bang profile, while the shallow FPA plot has a distinct transient region. We can also observe a similar trend of smaller ΔV s and shorter timespans for full-lift-up flight (i.e. flying at α_{\min}) as the FPA gets shallower. This behavior is expected due to the higher altitude periapsis that shallower trajectories would have.

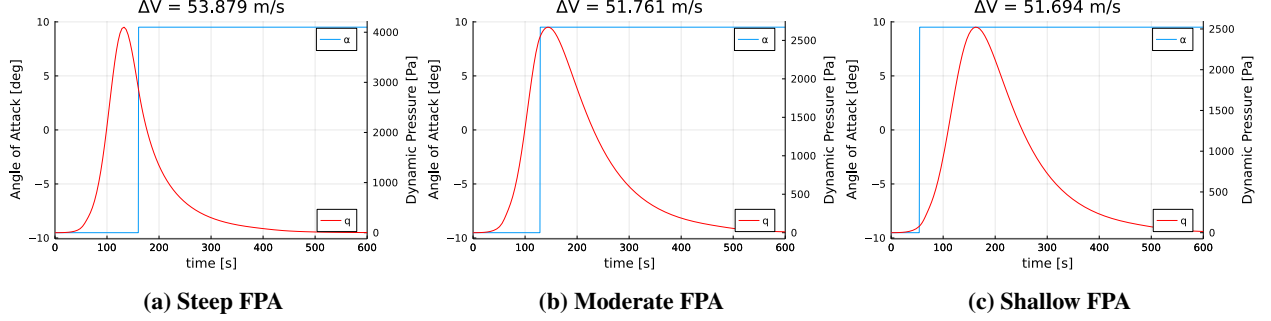


Fig. 8 Bang-Bang Profile with Various FPAs

Lastly, Figure 8 depicts results for the third approach: a fully bang-bang profile. We can first note that our angle of attack profiles and ΔV values for the steep and moderate FPA cases are nearly identical to those in Figure 7, as well as to the the fully discretized profiles in Figures 4c and 5c. We can also note that for the shallow FPA case, although our profile is different to that of the previous approaches, the ΔV is nearly the same. This provides evidence that even if a bang-bang profile is not truly the optimal angle of attack profile for a shallow FPA, it at least serves as a good approximation for the optimal profile.

B. Indirect Methods Results

Indirect methods were also applied to validate the direct method results. The two indirect method approaches derived in Section III were run here: a 2-burn, fixed-end-time formulation and a 1-burn, free-end-time formulation. Again, three different FPA cases are shown for each approach to analyze trends across the FPA corridor: a steep FPA, a moderate FPA, and a shallow FPA.

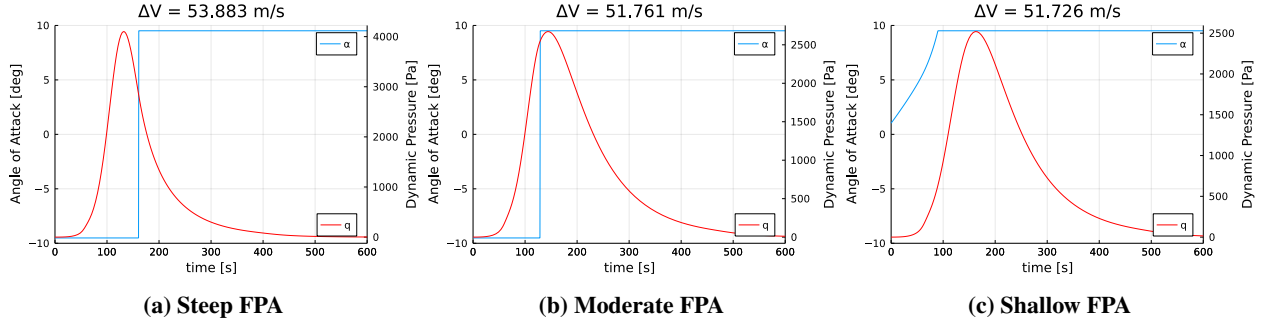


Fig. 9 2-Burn, Fixed-End-Time Approach with Various FPAs

Figure 9 depicts the results of the 2-burn, fixed-end-time formulation. We notice very similar results for the steep and moderate FPA cases, with profiles that appear bang-bang or nearly bang-bang (just as was the case for the direct methods). The shallow FPA case again appears to be the outlier, however we see a bit more nuance in the initial transient period. Without any assumptions on the linearity of the profile, we can see a somewhat parabolic trend during the initial transient period for the shallow FPA case.

Finally, Figure 10 shows the results of the 1-burn, free-end-time approach. Although each plot shows only the first 600 seconds of atmospheric flight for consistency, the values of t_f solved for by the optimizer are within 10 seconds of the direct methods for each FPA case. We notice nearly identical trends as in Figure 9, providing evidence to the validity

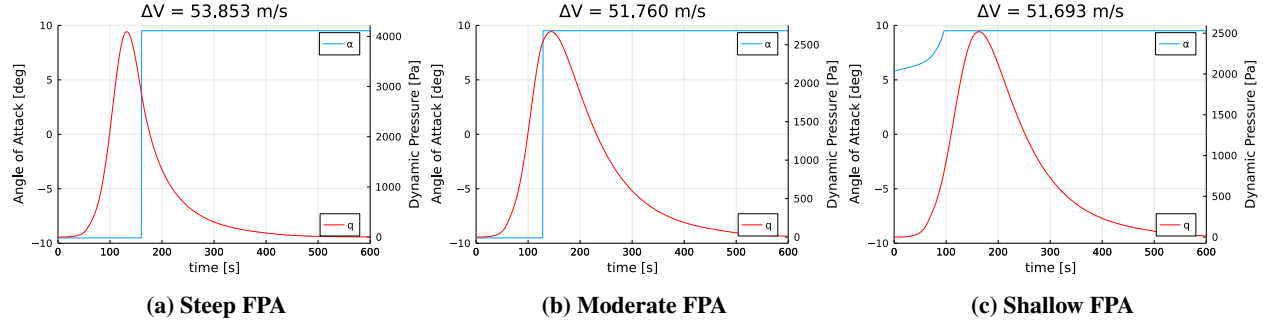


Fig. 10 1-Burn, Free-End-Time Approach with Various FPAs

of each of these indirect method approaches.

Table 2 summarizes the total ΔV s from the optimal trajectories for each optimization approach and each FPA. As can be seen, for a given FPA, all optimization approaches yield a ΔV to within 0.1 m/s of each other. This provides strong evidence that each of the different problem formulations are valid and are in close agreement. For the steep and moderate FPA cases, this shows that a bang-bang profile is likely to be optimal. For the shallow FPA case, even though the previous plots showed that the optimal profile may not be bang-bang, the similarity in final ΔV values suggests that a bang-bang profile provides a very good approximation of the optimal profile.

Table 2 Final ΔV Values for Each Optimization Approach

Approach	Total ΔV [m/s]		
	Steep FPA	Moderate FPA	Shallow FPA
Direct Methods			
Full Discretization ($N = 160$)	53.906	51.759	51.693
Near Bang-Bang	53.879	51.759	51.694
Bang-Bang	53.879	51.761	51.694
Indirect Methods			
2-Burn, Fixed-End-Time	53.883	51.761	51.726
1-Burn, Free-End-Time	53.853	51.760	51.693

V. Conclusions

Numerical methods were employed to determine the optimal angle of attack profile for aerocapture maneuvers using direct force control. Using optimal control theory and off-the-shelf numerical solvers, a bang-bang profile (full lift up then full lift down) was determined to be a good approximation for the optimal angle of attack profile. Though some results gave a clear indication of a bang-bang structure, others did not, likely due to low dynamic pressure (and therefore little aerodynamic control) towards the tail ends of the dynamic pressure curve. However, for a given FPA, a bang-bang structure provided similar ΔV values to other optimization approaches, providing further evidence that a bang-bang profile is likely close to the true optimum.

It was also found that 2-burn and 1-burn solutions yielded nearly identical results, meaning that for the chosen run configuration, the ΔV -optimal trajectory is one that explicitly targets the desired apoapsis, r_a^* . This implies that all of the ΔV is spent raising periapsis above the atmosphere, thus it is desirable to keep periapsis as high as possible (hence why steeper FPAs lead to larger ΔV s). Future work could address whether or not this conclusion holds for varying target orbit parameters. Additionally, scans across different vehicle properties, initial conditions, control bounds, planets, etc. could also shed more insight into whether or not a bang-bang angle of attack profile holds as a good assumption under all aerocapture conditions.

References

- [1] Cianciolo, A., and Powell, R., “Entry, Descent, and Landing Guidance and Control Approaches to Satisfy Mars Human Mission Landing Criteria,” *AAS/AIAA Space Flight Mechanics Conference*, 2017.
- [2] Matz, D. A., and Cerimele, C., “Development of a Numeric Predictor-Corrector Aerocapture Guidance for Direct Force Control,” *AIAA Scitech 2020 Forum*, 2020. <https://doi.org/10.2514/6.2020-0847>, URL <https://arc.aiaa.org/doi/abs/10.2514/6.2020-0847>.
- [3] Lu, P., Cerimele, C. J., Tigges, M. A., and Matz, D. A., “Optimal Aerocapture Guidance,” *Journal of Guidance, Control, and Dynamics*, Vol. 38, No. 4, 2015, pp. 553–565. <https://doi.org/10.2514/1.G000713>, URL <https://doi.org/10.2514/1.G000713>.
- [4] Deshmukh, R. G., Spencer, D. A., and Dutta, S., “Investigation of direct force control for aerocapture at Neptune,” *Acta Astronautica*, Vol. 175, 2020, pp. 375–386. <https://doi.org/https://doi.org/10.1016/j.actaastro.2020.05.047>, URL <https://www.sciencedirect.com/science/article/pii/S0094576520303313>.
- [5] Mall, K., and Taheri, E., “Unified Trigonometrization Method for Solving Optimal Control Problems in Atmospheric Flight Mechanics,” *AIAA Scitech 2020 Forum*, 2020. <https://doi.org/10.2514/6.2020-0022>, URL <https://arc.aiaa.org/doi/abs/10.2514/6.2020-0022>.
- [6] Pontryagin, L. S., Boltyanskii, V. G., Gamkrelidze, R. V., and Mishechenko, E. F., *The Mathematical Theory of Optimal Processes*, Intersciences, New York, 1962, Chap. 2.
- [7] Bryson, A. E., and Ho, Y.-C., *Applied Optimal Control: Optimization, Estimation, and Control*, 1st ed., Routledge, Boca Raton, 1975, Chap. 2, pp. 42–89. <https://doi.org/10.1201/9781315137667>.
- [8] Bezanson, J., Edelman, A., Karpinski, S., and Shah, V. B., “Julia: A fresh approach to numerical computing,” *SIAM review*, Vol. 59, No. 1, 2017, pp. 65–98. URL <https://doi.org/10.1137/141000671>.
- [9] Rackauckas, C., and Nie, Q., “DifferentialEquations.jl—a performant and feature-rich ecosystem for solving differential equations in julia,” *Journal of Open Research Software*, Vol. 5, No. 1, 2017.
- [10] Gill, P. E., Murray, W., and Saunders, M. A., “SNOPT: An SQP Algorithm for Large-Scale Constrained Optimization,” Vol. 47, No. 1, 2005, p. 99–131. <https://doi.org/10.1137/S0036144504446096>, URL <https://doi.org/10.1137/S0036144504446096>.